Core/Combustor-Noise Measurements and Source Separation for the DGEN Aeropropulsion Research Turbofan

Lennart S. Hultgren, Devin K. Boyle, and Brenda S. Henderson
Glenn Research Center, Cleveland, Ohio

NASA STI Program Report Series

Since its founding, NASA has been dedicated to the advancement of aeronautics and space science. The NASA scientific and technical information (STI) program plays a key part in helping NASA maintain this important role.

The NASA STI program operates under the auspices of the Agency Chief Information Officer. It collects, organizes, provides for archiving, and disseminates NASA's STI. The NASA STI program provides access to the NTRS Registered and its public interface, the NASA Technical Reports Server, thus providing one of the largest collections of aeronautical and space science STI in the world. Results are published in both non-NASA channels and by NASA in the NASA STI Report Series, which includes the following report types:

- TECHNICAL PUBLICATION.
  Reports of completed research or a major significant phase of research that present the results of NASA Programs and include extensive data or theoretical analysis. Includes compilations of significant scientific and technical data and information deemed to be of continuing reference value. NASA counterpart of peer-reviewed formal professional papers but has less stringent limitations on manuscript length and extent of graphic presentations.

- TECHNICAL MEMORANDUM.
  Scientific and technical findings that are preliminary or of specialized interest, e.g., quick release reports, working papers, and bibliographies that contain minimal annotation. Does not contain extensive analysis.

- CONTRACTOR REPORT.
  Scientific and technical findings by NASA-sponsored contractors and grantees.

- CONTRACTOR REPORT.
  Scientific and technical findings by NASA-sponsored contractors and grantees.

- CONFERENCE PUBLICATION.
  Collected papers from scientific and technical conferences, symposia, seminars, or other meetings sponsored or co-sponsored by NASA.

- SPECIAL PUBLICATION.
  Scientific, technical, or historical information from NASA programs, projects, and missions, often concerned with subjects having substantial public interest.

- TECHNICAL TRANSLATION.
  English-language translations of foreign scientific and technical material pertinent to NASA's mission.

Specialized services also include organizing and publishing research results, distributing specialized research announcements and feeds, providing information desk and personal search support, and enabling data exchange services.

For more information about the NASA STI program, see the following:

- Access the NASA STI program home page at http://www.sti.nasa.gov

NASA/TM-20240008331

Core/Combustor-Noise Measurements and Source Separation for the DGEN Aeropropulsion Research Turbofan

Lennart S. Hultgren, Devin K. Boyle, and Brenda S. Henderson
Glenn Research Center, Cleveland, Ohio

National Aeronautics and
Space Administration

Glenn Research Center
Cleveland, Ohio 44135

July 2024

Acknowledgments

Level of Review: This material has been technically reviewed by technical management.

This report is available in electronic form at https://www.sti.nasa.gov/ and https://ntrs.nasa.gov/

NASA STI Program/Mail Stop 050
NASA Langley Research Center
Hampton, VA 23681-2199

Core/Combustor-Noise Measurements and Source Separation for the DGEN Aeropropulsion Research Turbofan

Lennart S. Hultgren, Devin K. Boyle, and Brenda S. Henderson
National Aeronautics and Space Administration
Glenn Research Center
Cleveland, Ohio 44135

Abstract

Acoustic data obtained using a small turbofan engine are further analyzed with the aim to ultimately enable improved prediction methods and mitigation techniques for turbofan core/combustor noise. The relative impact of this propulsion-noise source for civilian-transport aircraft on airport community noise is expected to significantly increase in the future. Simultaneous high-data-rate acoustic measurements acquired using a circumferential infinite-tube-probe array at the core-nozzle exit in conjunction with a farfield microphone array are processed. The test matrix contains engine operational points from idle to engine-maximum setting, with measurements repeated for different circumferential array configurations, as well as for redundancy. The combustor-noise contribution to the farfield noise signature is obtained using an advanced source-separation method that correlates farfield microphone measurements with a modal decomposition of the unsteady pressure field at the core-nozzle exit. The advantages of the present approach compared to the classical two-signal source-separation method are discussed.

1 Introduction

The projected [1] evolution of turbofan design and advances in fan-noise mitigation imply that contributions from the combustor to the overall propulsion noise of civilian transport aircraft will increase in relative importance in the future. Consequently, a better understanding of turbofan core/combustor noise is needed so that effective noise-reduction strategies can be developed. In particular, it is crucial to understand the limitations that may be set by the core/combustor-noise component on future overall propulsion-noise reduction efforts. This is an issue of great environmental importance not only to future gas-turbine propulsors, but also to proposed far-term hybrid-electric aircraft-propulsion systems. Boyle et al. [2], which should be considered as a precursor to the current report, discusses these issues in more detail as well as puts the work in perspective with respect to the literature.

This report analyzes acoustic data from the July–August 2019 DGEN Aeropropulsion Research Turbofan (DART) source-diagnostic test (SDT) in the Aero-Acoustic Propulsion Laboratory (AAPL) at the NASA Glenn Research Center (GRC). The SDT campaign [2–4] continued the exploration and documentation of the DART core/combustor noise begun in an earlier baseline test [5]. However, now with more extensive instrumentation in order to answer questions raised by the previous investigation, as well as to further enhance the understanding of propulsion-noise sources and their impact on airport community noise resulting from the operation of civilian transport aircraft. The impetus for both tests is the need to ultimately develop improved prediction methods and mitigation techniques for turbofan core/combustor noise.

Section 2 gives a brief description of the experimental setup, instrumentation layout, and test matrix for the 2019-SDT campaign. More details are available in Hultgren et al. [4]. Furthermore, Boyle et al. [2] provides an uncertainty and error analysis. Simultaneous high-data-rate acoustic measurements are available from instrumentation that included a circumferential infinite-tube-probe (ITP) array at the core-nozzle exit in conjunction with sideline and farfield microphone arrays. The acoustic data obtained using the two sideline-array configurations are not discussed in the current report however. The engine operational points range from engine idle to maximum fan speed. The extensive data set (up to 93 channels of data, various configurations, and repeats for redundancy) allows the application of advanced source-separation and phased-array methods to elucidate not only the core-noise structure, but also the

propagation characteristics of other propulsion noise sources. Boyle et al. [2] evaluated the overall data quality and documented the modal structure of the unsteady pressure field at the core-nozzle exit. The present report evaluates the impact of this modal structure by presenting farfield narrowband sound-pressure-level (SPL) spectra for both the total-noise signature and the combustor-noise component. Combustor-noise results are obtained by the application of an advanced source-separation method that combines correlation methods with a mode-decomposition technique, eg. [6, 7], see Section 4 for details of the current approach. The advantages of the present approach over the 'classical' two-signal source-separation method as used in our previous work [5] are discussed.

2 Experiment

The DART testbed is a cost-efficient tool for the study of core-noise physics and mitigation. The center piece of this resource is an AKIRA MecaTurbines (Bayonne, France) DGEN 380 turbofan engine—originally developed, but not certified [8], by Price Induction for the personal-light-jet market. It is a two-spool 500 lbf (2.2 kN) thrust-class geared turbofan engine with a bypass ratio of approximately 7.6, a 3.32 fan gear ratio, a single centrifugal compressor on the high-pressure spool, a reverse flow annular combustor (jet-A fuel), and single stage uncooled axial high-pressure and low-pressure turbines. Its modular design allows the replacement of major components with parts modified for invasive instrumentation with comparative ease. Even though it is a rather small turbofan engine, its acoustic signature is relevant to large commercial aircraft engines [9, 10].

The testing took place within the AAPL facility at NASA GRC, which is an anechoic hemispheric dome with a radius of about 20m (65 ft) and acoustic treatment on the walls and floor. The treatment consists of fiberglass wedges, with a 0.61m (2 ft) depth, resulting in a design anechoic limit of approximately 150 Hz. The DART was positioned near the center of the facility allowing the use of the existing AAPL overhead microphone mounting points. Two alternate sideline microphone arrays (parallel to the engine center axis) and a core-nozzle circumferential array of differential pressure transducers, in ITP arrangement, near the nozzle exit were also deployed for the acoustic measurements. Figure 1 shows the DART and microphone arrays in AAPL. During normal operation the door on the far right is open to allow engine exhaust to exit the facility. The coordinate system used to describe measurement locations is a spherical one with its origin located on the engine centerline at the core-nozzle exit plane. The polar angle is zero in the inlet direction and the azimuthal angle is zero on the engine port-side (left-hand side facing forward) horizontal plane.

For each experimental configuration, the full authority digital engine control (FADEC) unit of the DART executed a program that runs through a sequence of predefined, monotonically increasing, engine-speed settings, with each set point held for 120 seconds. The speed setting corresponds to the ratio of the corrected fan speed on condition to that at a particular design point. Equivalently, it can be expressed in terms of low-pressure-spool shaft speeds as

$$engine\ speed = N_{\mathrm{L}}\sqrt{T_{\mathrm{SLS}}/T_{\mathrm{amb}}}/N_{\mathrm{Ld}}\ , \tag{1}$$

where $N_{\mathrm{L}}\sqrt{T_{\mathrm{SLS}}/T_{\mathrm{amb}}}$ is the temperature-corrected low-pressure-shaft speed and N_{Ld} is the design-point (corrected) shaft speed; N_{L} is the actual shaft speed, $T_{\mathrm{SLS}} = 288.15\,\mathrm{K}$ is the sea-level standard temperature, and T_{amb} is the ambient temperature (also in K) during a test point. The control program starts at ground idle (33%) and dwells at each of the speed settings 50, 60, 70, 80, 90, and $Max\,\%$, where $Max\,\%$ is a FADEC-enforced ambient temperature dependent maximum allowable corrected speed setting. It then returns to ground idle and the sequence is repeated once. The sequence additionally contains two test points with the engine off, but with support systems (such as the oil pump, etc.) running, for background-noise assessment. Boyle et al. [5] found that the engine under FADEC control performed quite repeatably in maintaining shaft speed for a given set point. The actual low-speed-shaft rotation rate, N_{L}, had an r.m.s deviation of less than 0.04% and its maximum observed deviation was less than 0.1%. Typical shaft-passing frequencies for the high-pressure spool, SPF_{H}, low-pressure spool, SPF_{L}, and the fan shaft, SPF_{F}, as well as blade-passing frequencies for the fan, BPF_{F}, and low-pressure turbine, BPF_{L}, are given in Boyle et al. [5, Table 3]. Of the blade-passing frequencies, only the BPF_{L} tone at the engine-idle speed setting falls within the 10 kHz frequency range.

2.1 *Unsteady Pressure Instrumentation Layout*

The core-nozzle-exit circumferential array consisted of eight ITPs, each instrumented with a Kulite® XCS-190-5D 5 psi (34.47 kPa) (Kulite Semiconductor Products Inc, Leonia, NJ) differential unsteady pressure transducer. The

Figure 1.   DART ①, sideline ② and overhead ③ arrays

ITP ports have a uniform 45-degrees azimuthal spacing. They are labeled NE801 through NE808, with the 'NE' indicating core nozzle exit. The circumferential-array arrangement has two variations. In the standard configuration, sensor port NE801 is in the twelve o'clock (90-degrees azimuthal) position and the numerical identifier increases in the counter-clockwise (positive-azimuthal) direction. In the clocked configuration, the circumferential array is simply rotated -22.5°. Further details can be found in Appendix A.1 as well as in Refs. 2 and 4.

All of the existing 24 microphone locations of the AAPL overhead array were utilized in this test. The microphones were oriented such that their faces pointed at the center of the core-exhaust plane. The overhead-array microphones are labeled as sensors FF001 through FF024, with the 'FF' indicating farfield and the numerical part increasing with aft position. Because the 'design origin' of the overhead-array is fixed within the AAPL and does not coincide with the origin at the nozzle-exit plane used here, both the radial distance from the engine-core exit and the azimuthal angle vary with the polar angle of the microphone position. However, the overhead microphones can be considered to be in the geometric farfield. The overhead array was populated with Brüel & Kjær type 4939 1/4-inch externally polarized free-field microphones. The polarization voltages were supplied by 6 four-channel Brüel & Kjær NEXUS 2690-A-OS4 microphone conditioning amplifiers. Each NEXUS channel was set to unity gain. The channels are A/C coupled by design, but have a number of selectable high-pass filters. The minimum cut-off frequency value of 0.1 Hz was used. Further details are available in Appendix A.2 and Refs. 2 and 4.

In addition to the microphones mounted in the overhead array, two alternate sideline 61-microphone arrays were also utilized in the SDT campaign [4]. However, the present report only utilizes acoustic data from the circumferential ITP array and the overhead microphone array. Consequently, no further details are presented here for the the two alternate sideline-array configurations.

2.2 *Data Acquisition and General Processing*

A total of 85 microphone signals and 8 ITP signals were simultaneously digitized at 100,000 samples per second utilizing a National Instruments[TM] (NI) PXIe-1082 chassis, populated with NI 4499 and 4498 analog-to-digital converter cards. The total observation time was 60 s at each experimental test point. Each individual time series thus contains about 6 million data points, i.e. 558 million data points were obtained for each test condition. In general, narrowband spectra were computed, as in [2, 5], using an FFT length of 16,384 points (corresponding approximately to a 6.1 Hz frequency resolution or binwidth), Hamming windowing, and a 50 percent data-segment overlap. Each resulting narrowband spectra are therefore the average of a large number of realizations (over 700 instantaneous spectra). Auto-spectra were computed using both the built-in capabilities of the NI LabVIEW software that is used to control the data acquisition and post-test using MATLAB scripts and routines. Cross-spectra, were computed using MATLAB with time-of-flight corrections applied to the microphone signals when appropriate.

Select engine mean-line data—such as ambient conditions, turbofan engine-station data, and engine-performance parameters—were recorded by an engine-data system at a sampling rate of 1 Hz. The engine-data system typically provided trigger events for the high-speed data-acquisition system at the beginning of each test-point sequence in order to determine the clock offset between the two systems.

3 Time of Flight

Typical (uncompensated) narrowband SPL results for the core-nozzle-exit location are illustrated in Fig. 2 for a frequency range of interest to combustor noise ($\lesssim$ 1.6 kHz). Panels (a)–(d) correspond to the engine-speed settings of 50, 60, 70, and 80%, respectively. The instrumented tailcone is in the standard configuration. Each panel shows the SPL spectra for the individual ITPs (solid lines—see legend), the SPL spectrum based on the averaged signal of the eight ITPs (dotted magenta line), and for comparison the FF019 farfield microphone (120° polar angle) SPL spectrum (dash-dot cyan line). The SPL spectra for the individual ITPs generally show similar behavior, except for the NE807 sensor (0° azimuthal position) which exhibits increased levels over a significant portion of the frequency range shown in these panels. This range also appears to extend to higher frequencies as the engine speed increases. The reason for this difference in behavior is not clear at present.

The dotted magenta SPL curves (based on the circumferential average of the ITP sensor signals) in Fig. 2 represent what a single sensor would have measured if only plane waves are present. In all of the four panels, this curve is a lower envelope for the individual-ITP curves up to about 600 Hz and then starts to trend away downwards. This implies that the modal structure at the core-nozzle exit is dominated by the plane wave up to about 600–800 Hz and that azimuthal (spinning and/or standing) modes come into play thereafter. On a qualitative basis, the results in the figure hints that the frequency at which this transition begins decreases somewhat as the engine speed is increased. See Table B 1, adopted from Boyle et al. [5], for estimated duct-mode cut-off/on frequencies at the core-nozzle exit.

As is well known, a time shift has to be applied to one of the signals when computing coherence to account for the propagation time between the measurement locations. A reliable coherence estimate is only obtained when the time histories are properly aligned. If the signals are only partially aligned, which would happen without time shifting if the 'time-of-flight' correction is less than a data-segment length or if an imperfect shift is applied, then the broadband coherence is underestimated. If the signals are unaligned, then only harmonic signals (tones) will have a nonzero coherence, i.e., estimated broadband coherence will fall below the value defined by the statistical confidence level. A time-of-flight correction is estimated here by subtracting the length of the ITP sense line from the radial coordinate of the farfield microphone and then dividing the result with the speed of sound. The adiabatic speed of sound is determined for each test point using the measured value for the ambient temperature. In addition, a small adjustment is allowed to empirically compensate for the speed of sound being slightly higher in the fan stream or in the ITP sense line. Since the acoustic propagation along the signal paths are essentially nondispersive (only exception would be while transversing shear layers), the cross-spectrum phase should exhibit a largely linear behavior in frequency bands where the signals are sufficiently coherent. A positive slope indicates a time lag. Consequently, the signals are properly aligned if the cross-spectrum phase is constant. This is how the additional time adjustment is determined here. It is important to note that the uncertainty in the estimated cross-spectrum phase increases as the coherence decreases (see Hultgren and Miles [11] for implications and Bendat and Piersol [12] for the uncertainty estimate).

Figure 3(a) shows the (unwrapped) cross-spectrum phase between the individual NE801–NE808 ITP sensors (solid lines), as well as the average of their signals (magenta dotted line), and the FF019 120° farfield microphone. The
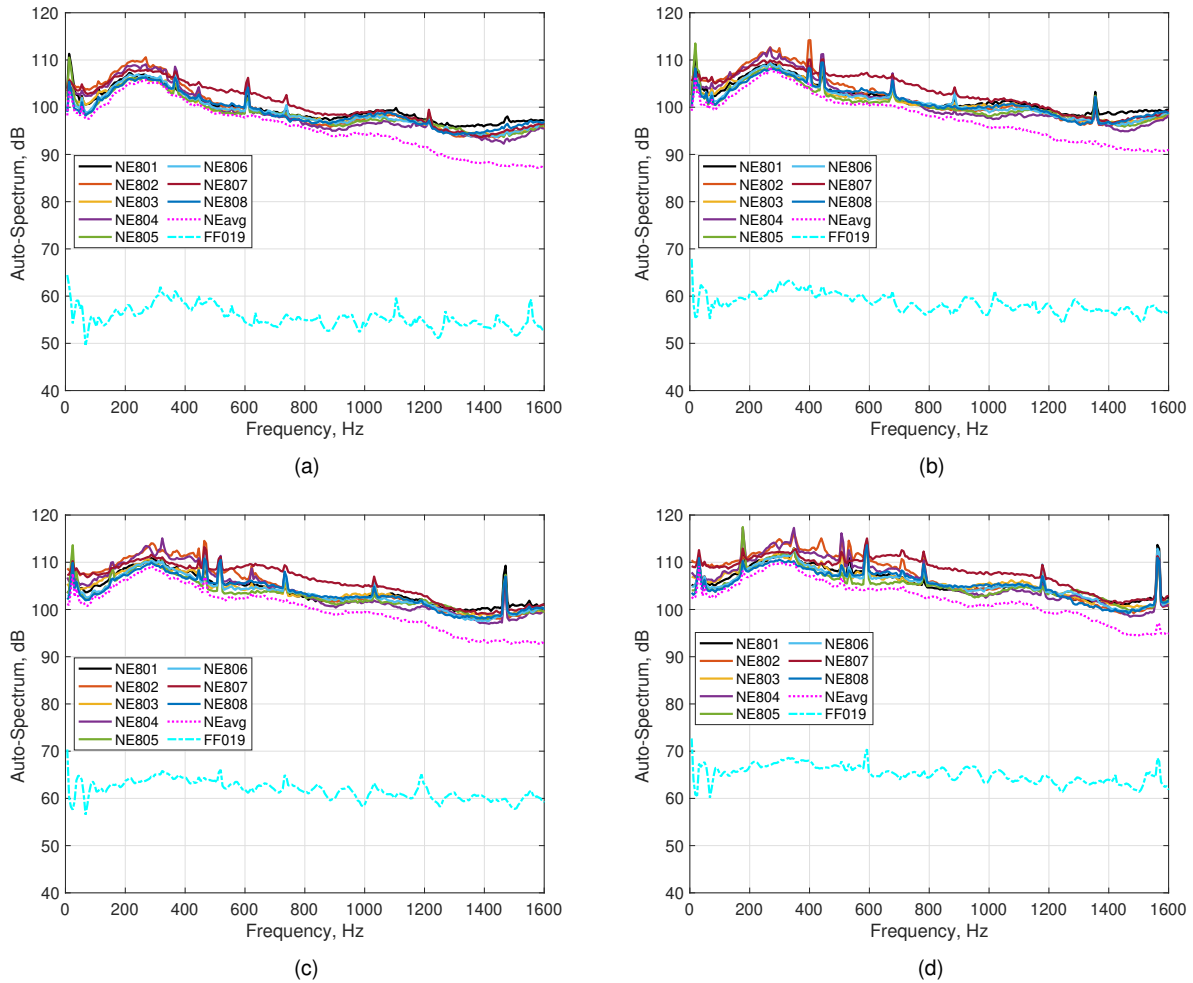
Figure 2.   Narrowband (6.1 Hz binwidth) SPL for the NE801–NE808 sensors at the core-nozzle exit and the FF019 farfield microphone (120° polar angle) versus frequency at (a) 50%, (b) 60%, (c) 70%, and 80% engine speed

dash-dot black line indicates the phase value of π radians. Qualitatively, the phases are all oscillating about this value (π) in a frequency range spanning from the anechoic limit (≈ 150 Hz) to first-azimuthal-mode cut-on (≈ 800 Hz). It follows that the radial coordinate of the farfield microphone is a good basis for estimating the time-of-flight from the core-nozzle exit to the farfield as long as the emanating acoustic waves are dominated by plane waves. Once an azimuthal structure can develop at the core-nozzle exit (roughly when the acoustic wave lengths start to become comparable to the nozzle diameter) the actual pressure-port location becomes important. This is evidenced by the positive slope, indicating an additional time delay, for the pressure ports located at the 'bottom side' of the nozzle for frequencies above the first-azimuthal-mode cut-on frequency. It turns out to be futile to attempt to establish robust individual time-of-flight estimates corresponding to the individual pressure ports since there is no approximate direct 'line-of-sight' for many of them.

The overall time-of-flight estimate used for the results shown in Fig. 3(a) is 29.98 ms ≈ 30 ms, i.e., the microphone time signal is shifted by 2998 data points. This estimate incorporates a built-in correction for the sense-line time lag of 3.54 ms and an added adjustment of -0.20 ms in order to make the curves qualitatively horizontal. This additional correction of 20 data points is very small compared to the data-segment length (16,384 data points) used in the signal processing routines. It follows that the additional adjustment has a negligible effect on estimated cross-spectrum magnitudes and, consequently, on coherence values to be presented below. However, it is needed in order to demonstrate adequate alignment of the signals. Figure 3(b) shows the cross-spectrum phase between the (circum-
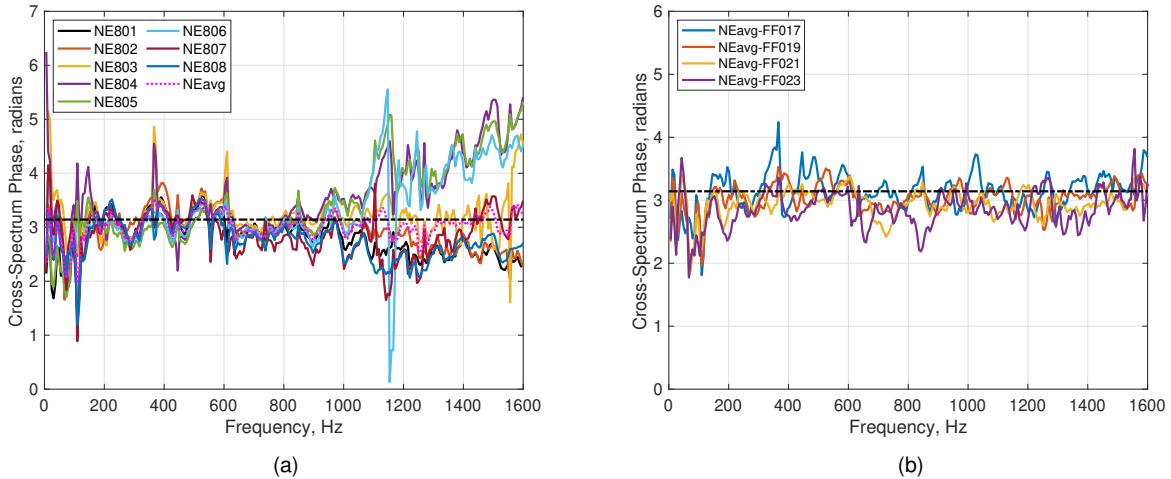
Figure 3.   Cross-spectrum phase at 50% engine speed (a) between individual ITPs (NE801–NE808), their average signal (NEavg), and the 120° farfield microphone (FF019) and (b) between the average ITP signal (NEavg) and the 108.7°, 120°, 131.9°, and 143.9° farfield microphones (FF017, FF019, FF021, FF023)

ferential) average ITP signal and four farfield microphones in the aft quadrant at the 50% engine-speed setting. The microphones (FF017, FF019, FF021, and FF023) are located in the 108.7°, 120°, 131.9°, and 143.9° polar directions. This figure demonstrates that the alignment procedure outlined above, with a fixed additional adjustment of -0.20 ms, works well in both the frequency range and polar-angle range of main interest for combustor noise.

4   Mode Decomposition and Source Separation
4.1   *Core-Nozzle-Exit Modal Structure*

Boyle et al. [2, 3] performed a modal decomposition of the unsteady pressure field at the core-nozzle exit based on the circumferential ITP-array measurements. Their previous work [5] had suggested that the first azimuthal duct mode, $(m,n) = (\pm 1, 0)$, where m and n denote azimuthal- and radial-mode orders, respectively, could be cut-on at this location, which would have implications for combustor-noise modeling and prediction. The mode-order index n indicates the number of pressure nodes (zeroes) in the radial profile. Their [2, 3] modal decomposition at the core-nozzle exit verified the presence of the first azimuthal mode.

Table B 1, adopted from Boyle et al. [2, Table 2], displays estimated duct-mode cut-off/on frequencies for various engine-speed settings. Based on the information in Table B 1, it follows that from a combustor-noise perspective (i.e. for frequencies up to about 1,600 Hz) only the first three azimuthal mode pairs, $(\pm 1, 0)$, $(\pm 2, 0)$, and $(\pm 3, 0)$, in addition to the always cut-on plane wave mode $(0,0)$, need to be resolved, which is within the capability of the circumferential ITP array used in the 2019-SDT campaign.

Circumferentially-averaged narrowband ITP SPL spectra, obtained by summing mean-squared pressures, are shown for the 0–1,600 Hz frequency range in Fig. 4. Panels (a) and (b) [2, Figs. 11 and 12] show the uncorrected and corrected SPL, respectively. Several *SPF* tones and harmonics can be identified. The only *BPF* tone occurring at a frequency low enough to potentially be observed in this range [2, 5] is $BPF_{\rm F} \approx 1,561$ Hz at 50% engine speed. A clear broadband hump (200-–500 Hz) is visible in the spectra at all engine-speed settings . Its peak value increases slightly slower than the overall spectra with engine speed. A second smaller broadband hump (around 1,100 Hz) is also visible in the spectra. Only the transfer-function correction accounting for viscous effects in an ideal line was applied to the results presented in Panel (b), see Boyle et al. [13] for more information. The details of the spectra are preserved but the general falloff with increasing frequency is reduced. Note that ITP transfer-function magnitude corrections cancel out for coherence-based source-separation methods. Only the ITP transfer-function phase lag needs to be accounted for in these methods and this can be accomplished through a simple signal time shift to leading (and sufficient) order.

Figure 5 shows the modal decomposition of the narrowband SPL at the circumferential-array location as well as their mean-pressure-squared sum for frequencies up to 1,600 Hz at 60% speed for (a) standard- and (b) clocked-array
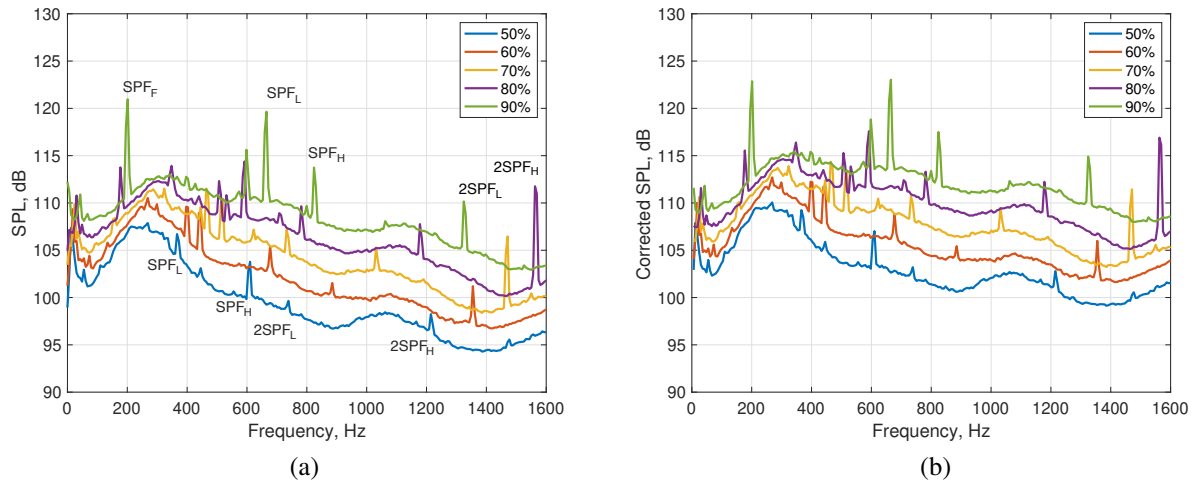
Figure 4. Circumferentially-averaged [2] narrowband (6.1 Hz binwidth) ITP SPL at the core-nozzle exit versus frequency at 60% speed setting—color coded as in legend: (a) raw spectra; (b) frequency-corrected spectra
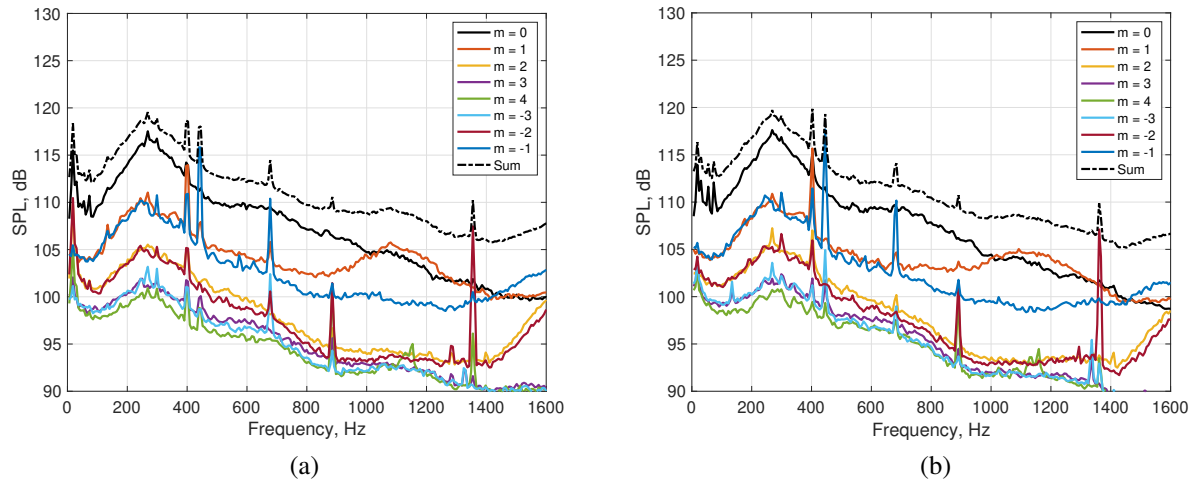

Figure 5. Modal contributions [2] to the narrowband (6.1 Hz binwidth) SPL at the core-nozzle exit versus frequency at 60% speed setting—color coded as in legend: (a) standard-array orientation; (b) clocked-array orientation

orientations [2, Figs. 19 and 20]. The 60% speed setting is a suitable representation of approach conditions where combustor noise is often prominent in practice. The reason for having two configurations for the circumferential array (standard and clocked) is that there are six support struts traversing the core nozzle near its exit. The struts are located in the 2, 4, ..., and 12 o'clock circumferential positions. Consequently, in the standard-array orientation, two of the ITP ports (NE801 and NE805) are directly downstream of struts. In the clocked configuration, no pressure ports are directly downstream of a strut.

The dot-dashed curve denoting the SPL sum in Fig. 5(a) matches the 60%-speed result in Fig. 4(a). The vertical offset between the two curves of $10\log_{10} 8 \,\mathrm{dB} \approx 9 \,\mathrm{dB}$ simply reflects the fact that one is a sum whereas the other is an average value. The overall features of the modal decomposition for the two configurations shown in Fig. 5 are generally comparable. The broadband SPL values, both circumferentially-overall (dot-dashed) and for individual modes, are essentially the same at lower frequencies, but start to deviate slightly at higher frequencies. The circumferential-overall SPL spectra are both dominated by the plane-wave mode contribution for frequencies below the estimated cut-on value for the ± 1 modes (just under 800 Hz), but are overtaken by the $m = 1$ mode at about 1 kHz. The $m = 1$

mode contribution significantly exceeds that of the $m = -1$ mode over a significant frequency range, especially after the point where the plane-wave mode loses its dominance, with the largest ± 1-mode difference occurring around 1,100 Hz. See Boyle et al. [2] for a discussion of possible reasons for this behavior. The $m = \pm 2$ modes are estimated, see Table B 1, to cut on at a value just under 1,600 Hz and their SPL contributions catch up with the plane-wave mode at about that frequency. This trend was also observed for $m = \pm 3$ modes [2], but their cut-on frequency is outside of the frequency range illustrated in this figure, however. Various tones and their harmonics are also captured in the individual modal SPL spectra.

Boyle et al. [2] concluded that the array orientation had no significant impact on the modal decomposition results since the modal content and cut-on indicators are largely unchanged between the two cases, with very similar, if not nearly identical, levels and trends.

4.2 *ITP-Array Modal Analysis*

Among others, modal decomposition using circumferential sensor arrays have been performed by Karchmer [14], Schuster and Mendoza [15], and Royalty and Schuster [16]. Karchmer [14] assumed standing waves in the azimuthal direction, i.e. equal amplitudes of the modes in each $\pm m$ pair, and solved for the amplitudes in a least-square sense. This approach has also been used by Krejsa and Karchmer [17] and Miles [18]. However, Schuster and Mendoza [15] and Royalty and Schuster [16] did not make the standing wave assumption and obtained the mode contributions by direct application of the discrete Fourier transform (DFT) in both the circumferential direction and time. This latter approach was followed by Boyle et al. [3] and is continued herein.

Consider the M time series, each containing N sample points,

$$u_n^{(l)} = u(\theta_n, t^{(l)}), \quad l = 0, 1, \ldots, N-1, \quad n = 0, 1, \ldots, M-1, \tag{2}$$

where $\theta_n = 2\pi n/M$, $n = 0, 1, \ldots, M-1$, are the circumferential sensor locations, $t^{(l)} = l/f_s$, $l = 0, 1, \ldots, N-1$ are times of the sample points, and f_s is the sampling rate. The DFT with respect to time of each sensor signal can be written as

$$U_n^{(k)} = \sum_{l=0}^{N-1} u_n^{(l)} e^{i2\pi kl/N}, \quad k = 0, 1, \ldots, N-1, \tag{3}$$

for each value of n. The superscript k is a frequency index, with the associated frequency given by $f^{(k)} = k f_s/N$. The corresponding inverse DFT is

$$u_n^{(l)} = \frac{1}{N} \sum_{k=0}^{N-1} U_n^{(k)} e^{-i2\pi kl/N}, \quad l = 0, 1, \ldots, N-1. \tag{4}$$

The DFT with respect to the azimuthal coordinate, θ, can be defined through

$$a_m^{(l)} = \sum_{n=0}^{M-1} u_n^{(l)} e^{-i2\pi mn/M}, \quad m = 0, 1, \ldots, M-1, \tag{5}$$

for each value of l. The index m represents the azimuthal wave number. The inverse given by

$$u_n^{(l)} = \frac{1}{M} \sum_{m=0}^{M-1} a_m^{(l)} e^{i2\pi mn/M}, \quad n = 0, 1, \ldots, M-1. \tag{6}$$

Using Eqs. (3)–(6) produces the forward and inverse double DFT pair

$$A_m^{(k)} = \sum_{l=0}^{N-1} \sum_{n=0}^{M-1} u_n^{(l)} e^{-i2\pi(mn/M - kl/N)}, \tag{7}$$

$$u_n^{(l)} = \frac{1}{MN} \sum_{k=0}^{N-1} \sum_{m=0}^{M-1} A_m^{(k)} e^{i2\pi(mn/M - kl/N)}. \tag{8}$$

Note that the opposite sign in the exponent is used in the azimuthal DFT compared to the time DFT. This means that a positive value of m corresponds to a wave traveling in the positive azimuthal direction.

It is relatively straightforward to show that

$$\sum_{n=0}^{N-1} |U_n^{(k)}|^2 = \frac{1}{M} \sum_{m=0}^{M-1} |A_m^{(k)}|^2, \tag{9}$$

for all k, i.e. frequencies. This relation is just another manifestation of Parseval's identity. Since $|U_n^{(k)}|^2$ represents the two-sided auto-spectrum of the signal u_n, it follows that $|A_m^{(k)}|^2/M$ is the auto-spectrum associated with the mode m.

The actual decomposition procedure generally follows Schuster and colleagues [15, 16]. For each time step, the azimuthal DFT, Eq. (5), is applied to the sensor-array data producing discrete time series for the modal amplitudes $a_m^{(l)}$. Second, the MATLAB routine `cpsd` is used to compute the auto-spectra for each mode, with Hamming windowing and 50% segment overlap. The results are renormalized (by M) in view of Eq. (9) and converted to one-sided spectra. Note that since the azimuthal DFT coefficients are cyclic, i.e. $a_{M+m}^{(l)} = a_m^{(l)}$, it follows that the spectra with the indexes $m = 1, 2, \ldots, M/2$ correspond to positive wave numbers in the usual sense and that the remaining spectra correspond to negative wave numbers through the reassignment $M-m \to -m$ for $m = 1, 2, \ldots, M/2-1$. Consequently, the modal-decomposition technique covers the $m = 0$ (plane wave), $\pm 1, \pm 2, \pm 3$, and $+4$ modes for the 2019-SDT circumferential array.

4.3 *Core/Combustor-Noise Component Identification*

As in Boyle et al. [5], identification of core-noise components of a total farfield-noise signature can be achieved through use of the classical two-signal coherence method [12, Ch. 4], also known as the coherent-output-power (COP) method. This method uses two signals, say $x(t)$ and $y(t)$, where the first is measured in the 'source' region and the other is measured at the location of interest. It is assumed that the source signal $x(t)$ is dominated by a single noise source, i.e., that other uncorrelated contributions to the measured signal are small and can be ignored. Such an assumption is not needed for the signal $y(t)$. The method is based on the magnitude-squared coherence between the signals

$$\gamma_{xy}^2 = \frac{|G_{xy}|^2}{G_{xx}G_{yy}}, \tag{10}$$

where G_{xy}, G_{xx}, and G_{yy} are the one-sided cross-power spectrum and auto-spectra of the two signals. All of the quantities involved are calculated from the recorded total noise signature data at the given locations. The COP method then provides the estimate

$$G_{vv} = \gamma_{xy}^2 G_{yy} \tag{11}$$

for the component G_{vv} of the total measured spectra, G_{yy}, at a location of interest that is coherent with a signal at another measurement (source) location.

Coherence, by definition (and in theory), ranges between zero and unity, where perfect coherence exists at the latter value. Perfect coherence implies a direct linear dependence of one signal on the other. A nonzero coherence value implies the dependence of both signals on a common source in the presence of other unrelated signals at both locations. A zero value implies that the two signals are independent. In practice, where the time series are always finite, a zero coherence value will not be achieved even for perfectly unrelated signals. A statistical estimate is then used to judge if the signals are uncorrelated. Any computed coherence value lower than this limit is not significant and the two signals are considered as fully independent. A 95% confidence level will be used for this estimate herein.

Davis and Bennett [6, 19] introduced a novel source separation approach that combines modal decomposition and coherence methods. One of several variations of this approach involves replacing one of the signals, or both, in the COP method with the complex signal corresponding to a specific cut-on duct mode. In most of the early applications of this technique [6, 19–22], cut-on duct modes at a location of interest were correlated with measurements by a single sensor in, or close to, a source region. However, in a later paper Pardowitz et al. [7] additionally determined the coherence between farfield microphone measurements and downstream propagating duct modes at the nozzle exit of a helicopter engine. This latter approach is carried out herein. This modal-COP technique extends the basic COP

analysis to frequencies where azimuthal duct modes are cut-on at the core-nozzle exit, i.e., where several mutually incoherent sources can be present.

Recently Sijtsma et al. [23] introduced a generalized coherent-output-power method utilizing groups of sensors, both at the source and farfield (or origin and target) locations. Their formulation allows for an arbitrary number of sensors in each group. The method also includes a denoising procedure for the origin sensors that can be applied if that group is sufficiently large. The denoising step can greatly improve the overall-method results. In the absence of denoising, their procedure essentially can be reduced for equispaced circumferential origin arrays to the modal-COP method used herein.

Hart et al. [24] introduced a modal-isolation extension to the so-called 3S-Array method. The 3S-Array method [25] is a three-signal coherence method [11, 26] where two of the sensors are engine internal and the third signal is the result of a phased-array beamforming technique where engine-external microphone measurements are focused on the core-nozzle exit. Replacing the two engine-internal single sensors with circumferential sensor arrays allows modal decomposition at the internal locations and thereby can extend the 3S-Array method to frequencies beyond the cut-off/on frequency of the first azimuthal duct modes [24]. Their paper [24] also discusses the effect of small errors in the positioning of the sensors in a circumferential array.

Finally, note that ITP transfer-function magnitude corrections, see Fig. A 2(a), cancel out for coherence-based source-separation methods. Only the ITP transfer-function phase lag, see Fig. A 2(b), needs to be accounted for in these methods and this can be accomplished through a simple signal time shift to leading (and here sufficient) order. See Boyle et al. [13] for information about the transfer function for the ITP design used here.
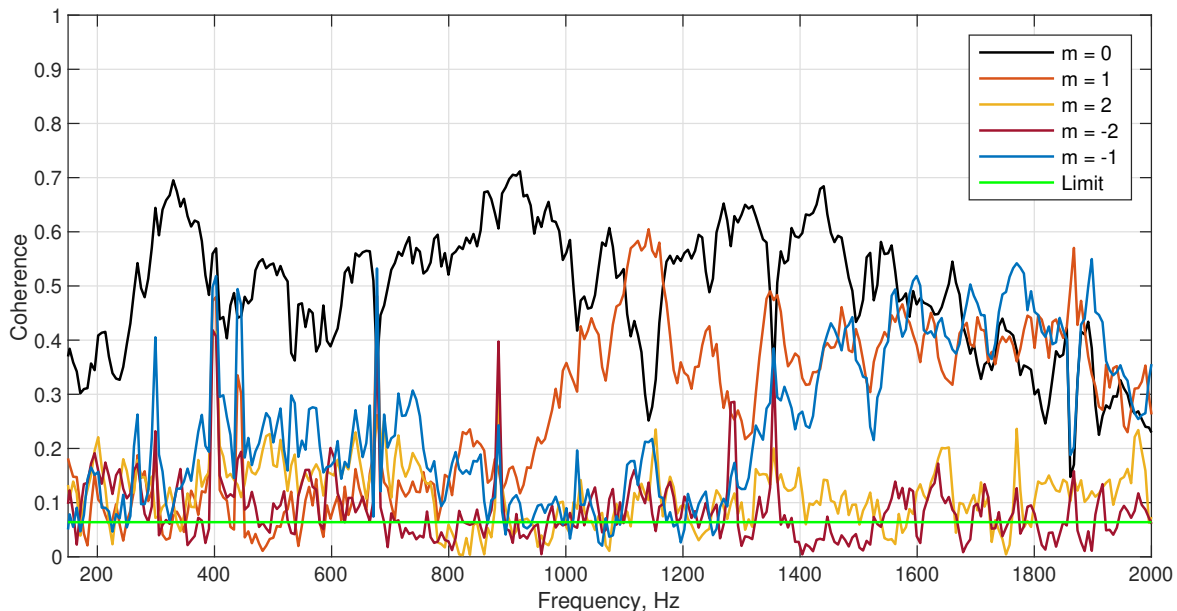
4.4 *Farfield Combustor Noise Component*

Figure 6.   Narrowband (6.1 Hz binwidth) coherence between core-nozzle-exit modes and the 120° farfield microphone (FF019) at 60% speed setting—$m = 0, \pm 1, \pm 2$, color coded as in legend; standard-array orientation

Figure 6 shows the coherence between the core-nozzle-exit modes ($m = 0, \pm 1, \pm 2$) and the acoustic signal at the 120° farfield microphone (FF019) at 60% engine speed. The green line represents the 95%-confidence limit for the coherence computation—for any frequency with a computed coherence value below this line the probability that the signals are uncorrelated is 95%. The broadband coherence values associated with the $m \neq 0$ modes are all subdominant
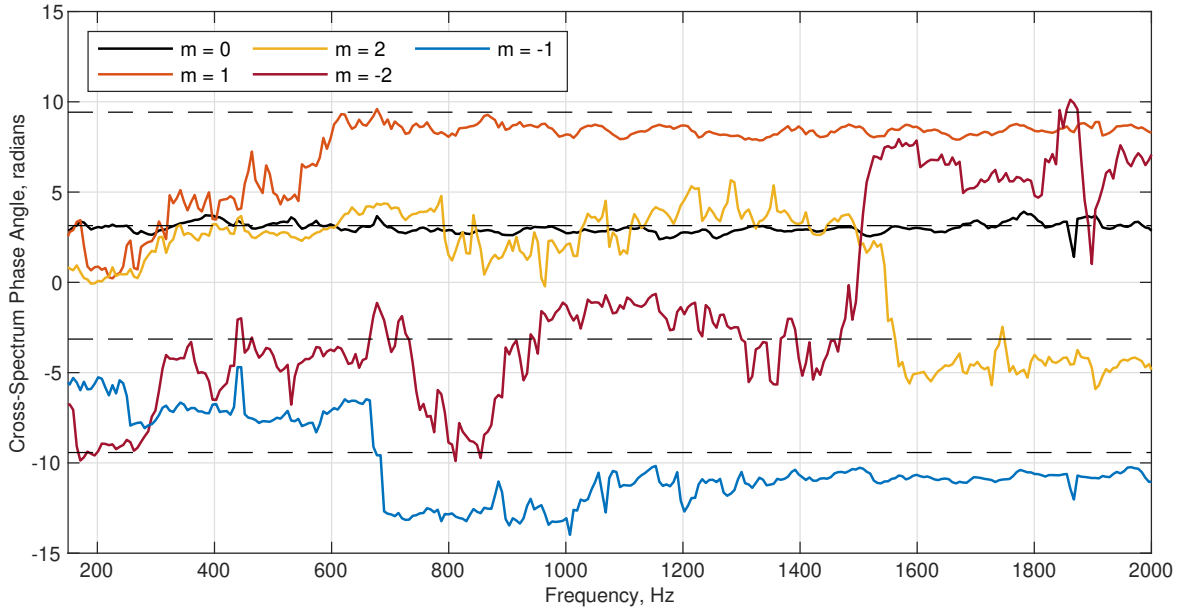
Figure 7. Narrowband (6.1 Hz binwidth) cross-spectrum phase angle between core-nozzle-exit modes and the 120° farfield microphone (FF019) at 60% speed setting—$m = 0, \pm 1, \pm 2$, color coded as in legend; standard-array orientation; dashed lines indicate $\pm\pi$ and $\pm 3\pi$
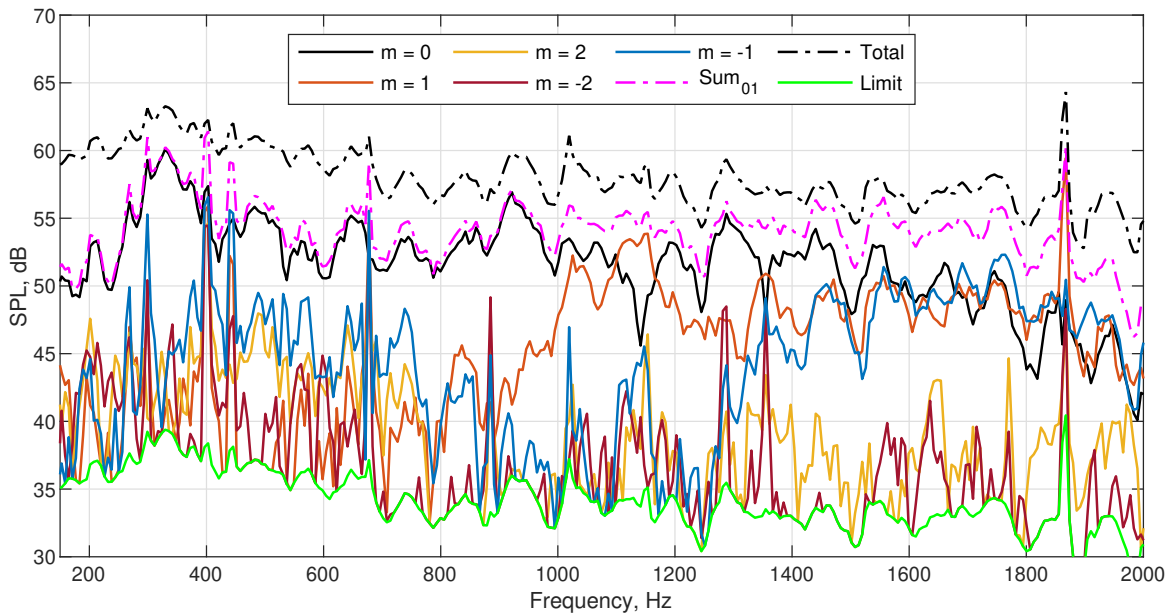

Figure 8. Modal contributions to the narrowband (6.1 Hz binwidth) SPL at the 120° farfield microphone (FF019) at 60% speed setting—total noise signature, $m = 0, \pm 1, \pm 2$, color coded as in legend, dotted magenta line: cumulative contribution from $m = 0, \pm 1$; standard-array orientation

for frequencies less than about 1 kHz. The tonal contributions to the coherence, in this frequency range, can mostly be associated with low- and high-spool shaft frequencies (SPF_L and SPF_H) and harmonics, see Fig. 4(a) or Ref. [2, Table 1]. The broadband coherence values associated with the $m = 1$ and the $m = -1$ modes become significant around 1 kHz and 1.4 kHz, respectively, whereas the corresponding values for the $m = \pm 2$ modes do not start to increase until close to 2 kHz.

Figure 7 shows the phase angle of the cross-spectrum between the core-nozzle-exit modes ($m = 0, \pm 1, \pm 2$) and the acoustic signal at the 120° farfield microphone (FF019) at 60% engine speed. For $m = 0$, the phase angle is essentially constant over the frequency interval depicted in this figure. For $m = 1$, the phase angle becomes 'constant' around 600–800 Hz, i.e., just before mode cut-on. For unknown reasons, the phase angle for the $m = -1$ mode does not level out until about 1.4 kHz, which is in agreement with the coherence results shown in Fig. 6. Having a constant, or near constant, value for the phase angle is a necessary, but not sufficient, condition for significant broadband coherence between the signals since it indicates that they are properly aligned in time. Note that the $m = 2$ phase angle is nearly constant over most of the frequency range shown in the figure (also the phase change of about 2π roughly at mode cut-on is not physically relevant), but its broadband coherence is still relatively insignificant.

Figure 8 shows the modal ($m = 0, \pm 1 \pm 2$) contributions to the total SPL at the 120° farfield microphone (FF019), as computed with the modal coherent-output-power method. The dotted magenta line represents the cumulative contribution of the $m = 0, \pm 1$ modes. The dash-dotted black line is the acoustic signature measured at the FF019-microphone location. For frequencies less than about 1 kHz, the $m = 0$, i.e., plane-wave, mode is clearly dominant. Above that frequency, the contributions from the $m = \pm 1$ modes become appreciable. Above about 1.5 kHz, the contributions to the SPL from $m = 0, \pm 1$ are of comparable magnitude.
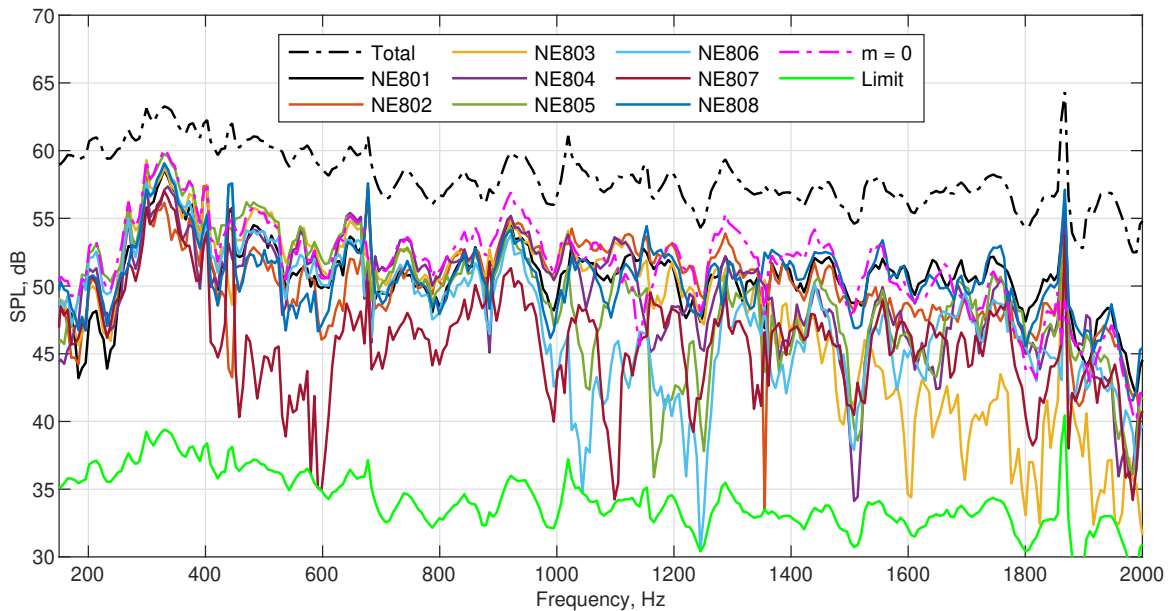

Figure 9. Estimated contributions to the narrowband (6.1 Hz binwidth) SPL at the 120° farfield microphone (FF019) at 60% speed setting—total noise signature, estimates using an individual core-nozzle-exit ITP-sensor signal or the average of the ITP signals ($m = 0$ mode) as inputs, and 95%-confidence limit; standard-array orientation

Figure 9 compares the estimated contribution of the core-nozzle-exit unsteady pressure field to the total acoustic signature (dot-dashed black line) at the 120° microphone (FF019), as computed with the two-signal coherent-output-power method, using each individual core-nozzle-exit ITP sensor (solid color lines as indicated in the legend) as well as the $m = 0$ mode (dot-dashed magenta line) as the input signal. The $m = 0$ result is, of course, equivalent to what

would be obtained if the average of the ITP-sensor signals are used as the input to the method. The result based on the NE807 sensor is also here an outlier—as is likewise evident in Fig. 2. It is conceivable that engine-performance instrumentation protruding into the fan stream at the 9-o'clock position [5, Fig. 3] could cause a local nonuniformity in the core/fan-stream shear layer, thus affecting the acoustic wave radiation pattern downstream of the NE807-sensor port. However, it is more likely that the higher SPL levels for NE807 shown in Fig. 2 are related to a yet unidentified uncorrelated noise source since then the positive-bias error inherent to the two-signal method (see eg. [11, 12] and references therein) would lead to an underprediction of the farfield contribution—just as seen in Fig. 9.
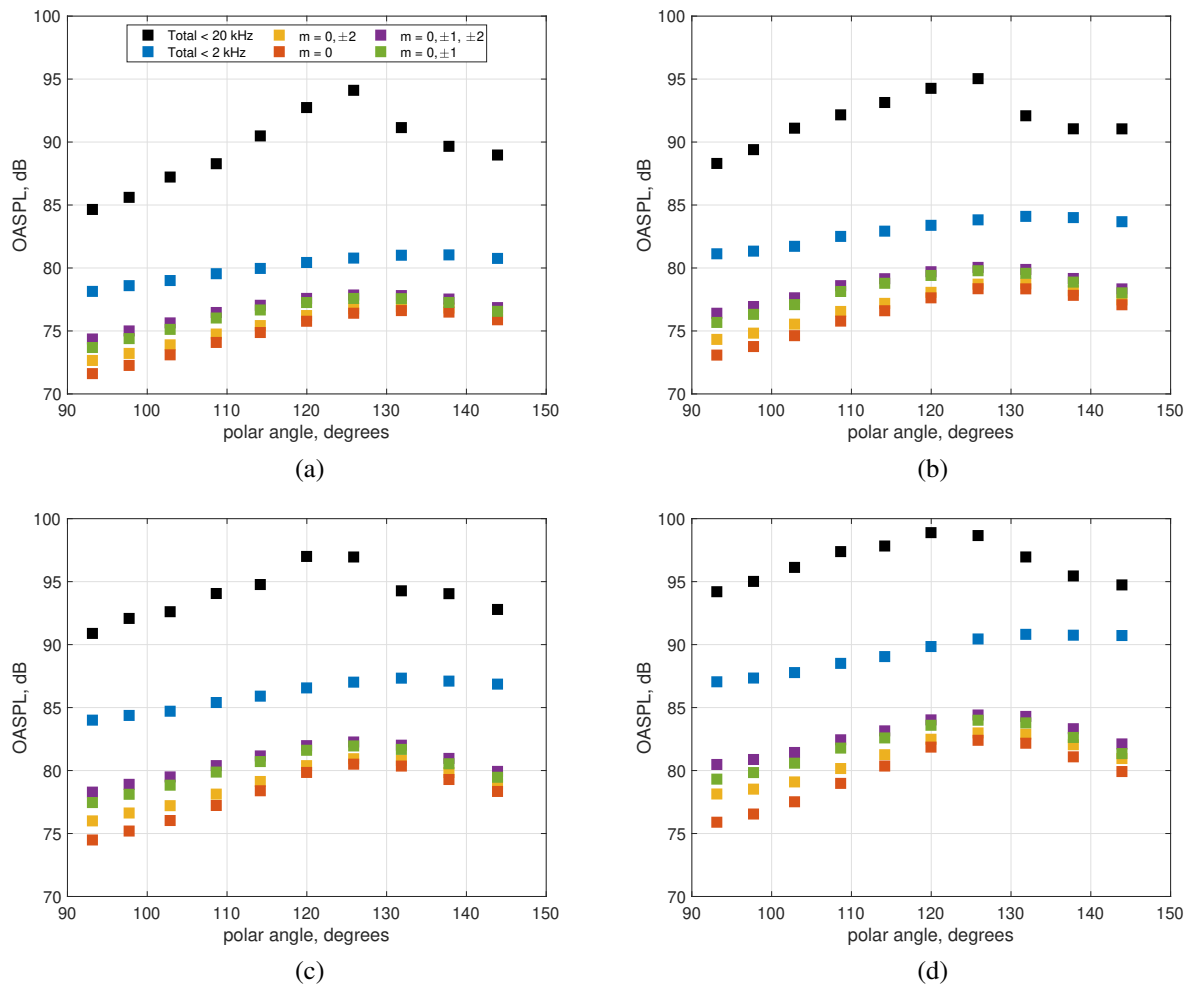

Figure 10. Modal-COP estimates of core/combustor-noise contributions—color coded as in legend—to the OASPL versus polar angle on an engine-aft arc of fifty core-nozzle diameters radius at various engine speeds: (a) 50%; (b) 60%; (c) 70%; (d) 80%

Figure 10 shows the estimated overall sound pressure level (OASPL) associated with combustor noise in the engine aft sector for the four engine-speed settings of 50%, 60%, 70%, and 80%. The data has been corrected for spherical spreading to correspond to an arc passing through the $120°$ microphone location, which is approximately at a distance of fifty core-nozzle diameters. The black symbols indicate the OASPL based on the total noise signatures measured by the farfield microphones in the frequency range of 150 Hz to 20 kHz. The blue symbols denote the corresponding total results but with the upper frequency limit reduced to 2 kHz. The red, yellow, green, and purple symbols represent the estimated core/combustor-noise contributions to the farfield noise signature from the $m = 0$, $m =$

$0, \pm 2$, $m = 0, \pm 1$, and $m = 0, \pm 1, \pm 2$, mode combinations, respectively. These estimates were obtained by summing up modal-COP results from 150 Hz–2 kHz. Clearly identifiable tonal contributions were excluded from the summations in the 150–800 Hz and 150–1,600 Hz ranges for the $m = \pm 1$ and $m = \pm 2$ modes, respectively. As can be seen in the figure, the $m = \pm 1$ and $m = \pm 2$ modes contribute at all of the polar angles shown, but increasingly so as broadside angles are approached and as the engine speed is increased. The peak combined modal-contribution to the farfield noise signature occurs for a polar angle of roughly $125°$.

For the plane-wave ($m = 0$) mode contribution, a second-order polynomial was fitted to the data—using five points, with two on each side of the maximum educed OASPL contribution—to obtain a better estimate of the peak polar angle. This procedure yielded the estimated peak polar angles for the plane-wave mode of $132.4°$, $129.4°$, $127.6°$, and $127.2°$ for the engine-speed settings of 50%, 60%, 70%, and 80%, respectively. These values should be compared to the model implemented in the GECOR combustor-noise module in the NASA Aircraft Noise Prediction Program (ANOPP) [27, 28]. In this model [29], the peak directivity polar angle is a constant $120°$ for all operational points.

Figure 11 illustrates the directivity of the educed core/combustor-noise over a partial range of downstream polar angles ($90–150°$). The symbols in Fig. 11(a) denote the ANOPP-GECOR model values and the dot-dashed curve represents a partial spline fit. Figure 11(b) illustrates the normalized directivity index, obtained from the OASPL contribution, for the plane-wave mode at various engine-speed settings (see legend) as well as the ANOPP-GECOR partial spline fit. The normalized directivity index is given by $\mathrm{DI}(\theta) = \mathrm{OASPL}(\theta) - \mathrm{OASPL}(\theta_{max})$, where θ_{max} is the peak directivity polar angle. The abscissa is expressed as a normalized polar angle in both of the (a) and (b) panels in Fig. 11. Not only are the peak angles larger than in the ANOPP-GECOR model, the normalized directivity-index functional shapes are also broader. However, as the engine-speed setting is increased, the educed normalized directivity index approaches that of the ANOPP-GECOR model.
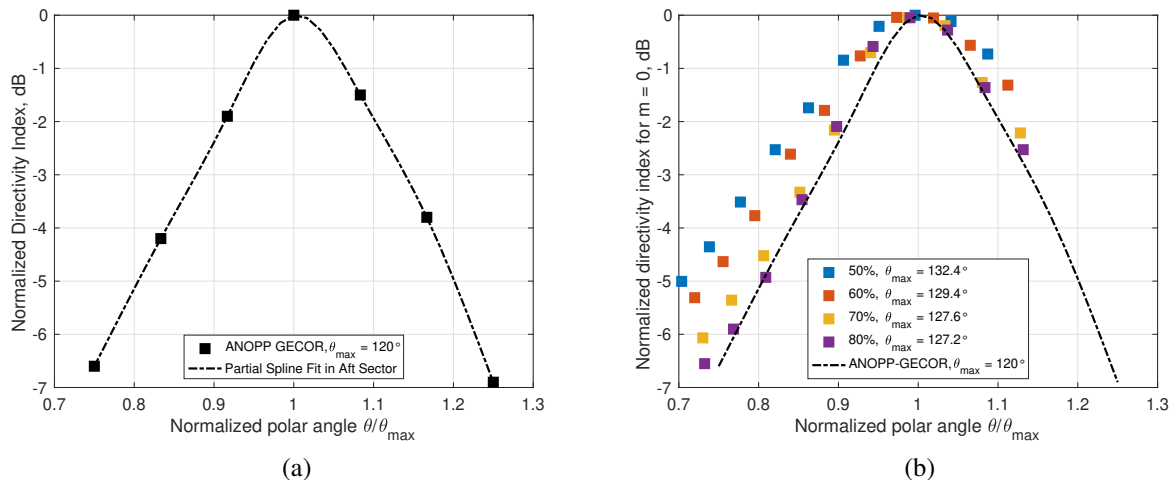

Figure 11. Plane-wave ($m = 0$) aft-sector normalized directivity index: (a) ANOPP-GECOR model; (b) data at 50%, 60%, 70%, and 80% engine speeds

5 Summary and Conclusions

Acoustic data from the July–August 2019 DGEN Aeropropulsion Research Turbofan test carried out in the Aero-Acoustic Propulsion Laboratory at the NASA Glenn Research Center has been analyzed. The test campaign [2–4] continued the exploration and documentation of the DGEN 380 core/combustor noise begun in an earlier baseline test [5], but with more extensive instrumentation, in order to answer questions raised by the previous investigation, as well as to further enhance the understanding of propulsion-noise sources and their impact on airport community noise resulting from the operation of civilian transport aircraft.

A modal coherent-output-power method was used to estimate the combustor-noise contribution to the farfield noise signature of the DGEN 380 turbofan engine. A significant advantage of the modal formulation is that it can minimize the inherent bias error in the coherent-output-power method. The classical method assumes that any part of the signal at the origin location (here, the core-nozzle exit) that is not coherent with the signal at the target location is very small and can be neglected. Furthermore, it is assumed the signal is due only to *one* source. For sufficiently low frequencies, only the plane-wave mode can propagate in the engine-internal core duct and this latter requirement is satisfied. As the frequency increases, however, successive azimuthal duct modes become cut on. As this happens, the classical method will at first underestimate the contribution at the farfield, due to its inherent bias issue, but ultimately it will fail to yield meaningful results. If the azimuthal modes originated in the combustor, they will be statistically independent from the plane wave and each other, with the likely exception that modes with opposite but equal azimuthal wave numbers might form standing waves in the circumferential direction. If the azimuthal modes are formed by scattering of the plane wave by the turbomachinery or duct support structures, then they might be partially, but not fully, coherent with the plane wave. Nevertheless, the diagnostic capability of classical method deteriorates as the single-source assumption is violated. The modal-decomposition technique alleviates this problem by performing the coherent-output-power computation on a per mode basis.

The application of the modal coherent-output-power method to the data showed that the plane-wave mode is the dominant contributor to the farfield noise signature at low frequencies. As expected, contributions associated with the azimuthal duct modes started to successively become important at frequencies consistent with their estimated cut-on/off values and ultimately their impact became of comparable magnitude to that of the plane-wave mode. Somewhat contrary to expectation, the plane-wave contribution did not greatly diminish as the first azimuthal mode pair started to contribute to the farfield noise signature—rather it showed a gradual reduction with frequency.

The contributions from the azimuthal modes were found to be comparable in magnitude to the plane-wave mode contribution in the peak direction of core/combustor-noise. Their importance increased as broadside angles were approached, however. The peak polar directivity angle of the core/combustor-noise contribution was found to be generally consistent with prediction models, albeit slightly larger.

APPENDICIES

A Instrumentation Layout

A.1 *Core-Nozzle-Exit Circumferential Array*

Eight ITPs, each instrumented with a Kulite® XCS-190-5D 5 psi (34.47 kPa) (Kulite Semiconductor Products Inc, Leonia, NJ) differential unsteady pressure transducer, were installed at the core-nozzle exit providing engine-internal measurements. Figure A 1 shows the DART with the instrumented tailcone installed, with panel (c) schematically showing the location of the ITP ports in more detail. The ITP ports are labeled NE801 through NE808, with the 'NE' indicating (core) nozzle exit and have a uniform 45-degrees azimuthal spacing. In the standard configuration, sensor port NE801 is in the twelve o'clock (90-degrees azimuthal) position and the numerical identifier increases in the counter-clockwise (positive-azimuthal) direction in the panel (c) view. There are two additional instrumentation ports, offset ± 22.5 degrees from the NE801 port, allowing for supplementary instrumentation. In the alternate clocked configuration, the circumferential array (i.e., the tailcone) is simply rotated -22.5°.

The ITP sense lines are 1.22 m (48 inch) long. They are routed, see Fig. A 1, through the core-nozzle center body into a simple symmetric airfoil while crossing the core and fan streams, each leading to a block where a pressure transducer is flush-mounted to the inner wall of the sense line. On the other side of each transducer tee is a 15.24 m (50 ft) long 'infinite' line with a capped termination. This line is sufficiently long to eliminate effects on the measurements by reflections from the end conditions, see Boyle et al. [13]. The inner diameter of 4.93 mm (0.194 inch) is maintained throughout to avoid pressure reflections/distortions. Each transducer's reference-pressure side is vented to atmospheric conditions. The ideal transfer function for this ITP design is illustrated in Fig. A 2. Based on the results in Boyle et al. [13], the use of this approximation is adequate for the present situation. Note that the straight-line phase lag shown in Fig. A 2(b) implies a constant transducer-signal time delay relative to the desired measurement location.

The pressure transducers were provided constant-voltage excitation by a Precision 28118-FX02-LP4FP-T 8-channel bridge-conditioner card. Six-wire cables were employed for each channel, with the three pairs providing excitation voltage, excitation monitoring, and signal transfer. This card also performed analog gain, with its built-in programmable lowpass filter bypassed, prior to the transducer output signals entering the ADC system.
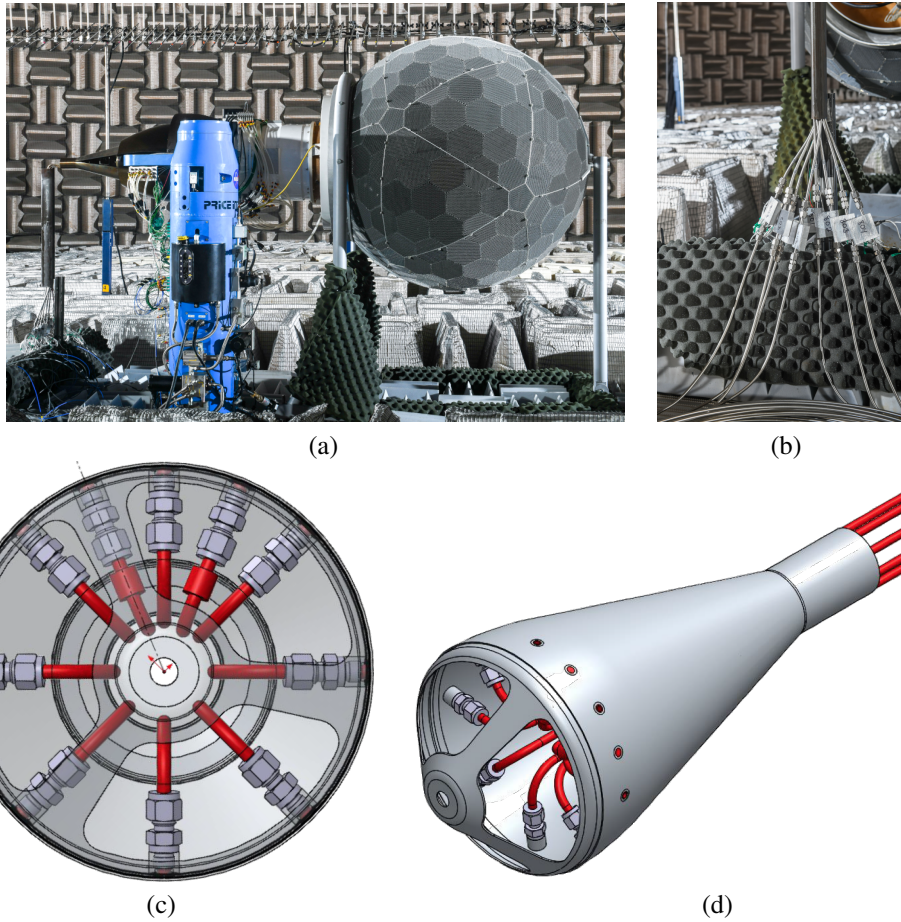
Figure A 1.   (a) DART with instrumented tailcone; (b) ITP transducer tees; (c) tailcone instrumentation ports, downstream view; (d) tailcone schematic
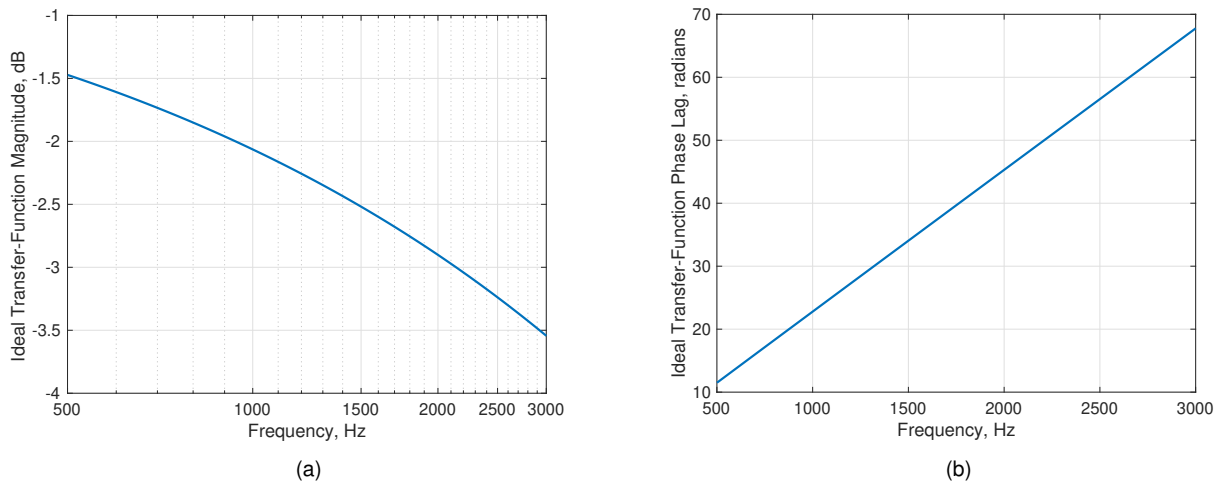

Figure A 2.   Ideal ITP transfer function [13]: (a) – magnitude; (b) – phase lag

A.2 Farfield (Overhead) Microphone Array

The microphones, in the existing 24 microphone locations of the AAPL overhead array, were oriented such that their faces pointed at the center of the core-exhaust plane. The overhead-array microphones are referred to as sensors FF001 through FF024, with the 'FF' indicating farfield and the numerical part increasing with aft position. The microphone locations are given in Table A 1.

Table A 1. Farfield microphone locations in spherical coordinates

| microphone	radius, ft	radius, m	polar, °	azimuth, °	microphone	radius, ft	radius, m	polar, °	azimuth, °
FF001	54.66	16.66	41.76	117.35	FF013	42.67	13.01	87.57	86.38
FF002	55.37	16.88	44.04	111.71	FF014	41.64	12.69	93.13	85.46
FF003	53.41	16.28	46.97	108.48	FF015	41.09	12.52	97.73	84.70
FF004	52.25	15.92	50.55	104.91	FF016	40.18	12.25	102.87	83.92
FF005	51.18	15.60	53.85	101.81	FF017	39.40	12.01	108.65	83.42
FF006	49.97	15.23	57.12	98.71	FF018	38.71	11.80	114.17	82.23
FF007	49.01	14.94	60.94	96.46	FF019	38.15	11.63	119.97	83.17
FF008	48.36	14.74	64.77	93.51	FF020	37.46	11.42	125.87	83.36
FF009	47.01	14.33	69.11	92.44	FF021	36.98	11.27	131.85	84.15
FF010	45.85	13.97	73.56	89.99	FF022	36.60	11.16	137.81	85.01
FF011	44.62	13.60	78.06	88.60	FF023	36.56	11.14	143.90	87.56
FF012	43.91	13.38	83.01	87.67	FF024	36.32	11.07	149.71	90.34

(a)

(b)
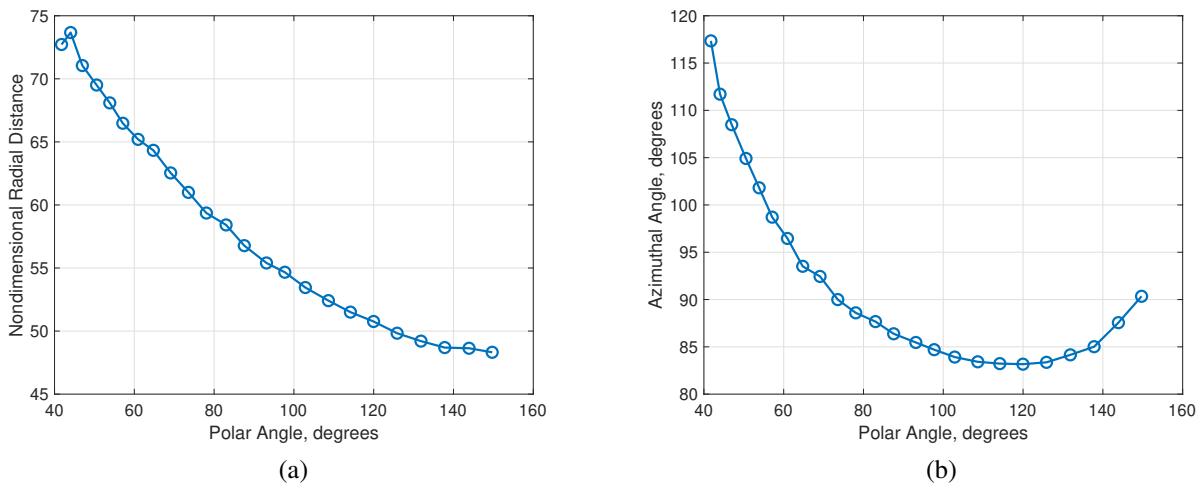
Figure A 3. AAPL overhead array: (a) microphone nondimensional radial distance versus polar angle; and (b) microphone azimuthal angle versus polar angle

Figure A 3(a) and (b) show the radial distance, normalized by the core-nozzle-exit diameter, and the azimuthal angle versus the polar angle for the microphones. The polar angles fall in the approximate range of 42–150 degrees. Note that both the radial distance from the engine-core exit and the azimuthal angle vary with the polar angle of the microphone position since the 'design origin' of the overhead-array is fixed within the AAPL and does not coincide

with the origin used here. The (nondimensional) radial distance falls in the range of about 48–74. Thus, according to the criteria given by Ahuja [30], the overhead microphones can be considered to be in the geometric farfield. The azimuthal angles of the overhead-array microphones vary due to the out-of-azimuthal-plane rotation of the array in the current coordinate system.

The overhead array was populated with Brüel & Kjær type 4939 1/4-inch externally polarized free-field microphones. The polarization voltages were supplied by 6 four-channel Brüel & Kjær NEXUS 2690-A-OS4 microphone conditioning amplifiers. Each NEXUS channel was set to unity gain. The channels are A/C coupled by design, but have a number of selectable high-pass filters. The minimum cut-off frequency value of 0.1 Hz was used.

B   Core-Nozzle-Exit Modal Cut Off/On Frequencies

Table B 1, adopted from Boyle et al. [2, Table 2], displays estimated duct-mode (m,n) cut-off/on frequencies for various engine-speed settings at the core nozzle exit. The duct mode indices m and n denote the azimuthal and radial mode orders, respectively, with the latter indicating the number of pressure nodes (zeroes) in the radial profile. Meanline conditions, such as the local Mach number and speed of sound, from an engine-deck simulation for the DGEN 380 turbofan were used to determine the physical frequencies. A mode (m,n) can only propagate for frequencies higher than its cut-off/on frequency. The plane-wave mode (0,0) can always propagate. Of note is the fact that the cut-off/on frequencies for all radial mode orders, $n > 0$, are well outside of the range of interest from a combustor-noise perspective. The relatively small ratio of the annular-duct height to its outer radius ($= 0.195$) is the reason for the high radial-mode cut-off/on values. In fact, modes with $\pm m = 1$–14 are successively cut on before the first radial mode (0,1) is cut on [5]. Based on the information in Table B 1, it follows that from a combustor-noise perspective (i.e. for frequencies up to about 1,600 Hz) only the first three azimuthal mode pairs, $(\pm 1,0)$, $(\pm 2,0)$, and $(\pm 3,0)$, in addition to the always cut-on plane wave mode $(0,0)$, need to be resolved, which is within the capability of the circumferential ITP array used in the 2019-SDT campaign.

Table B 1.   Estimated duct-mode cut-off/on frequencies (Hz) at the core-nozzle exit [2, 5]

Engine Speed		n=0	n=1	n=2	n=3
60 %	m=0	0	11,532	23,033	34,541
	m=1	793	11,559	23,047	34,550
	m=2	1,586	11,642	23,088	34,577
	m=3	2,378	11,779	23,157	34,623
70 %	m=0	0	11,491	22,951	34,417
	m=1	790	11,518	22,964	34,426
	m=2	1,580	11,601	23,005	34,454
	m=3	2,370	11,738	23,074	34,500
80 %	m=0	0	11,465	22,900	34,341
	m=1	789	11,493	22,913	34,350
	m=2	1,577	11,575	22,954	34,377
	m=3	2,365	11,711	23,023	34,423
90 %	m=0	0	11,414	22,797	34,187
	m=1	785	11,441	22,810	34,196
	m=2	1,570	11,523	22,851	34,223
	m=3	2,355	11,659	22,919	34,268

REFERENCES

[1] L. Mongeau, D. Huff, and B. J. Tester. Aircraft noise technology review and medium and long term noise reduction goals. In *Proceedings of Meetings on Acoustics*, volume 19, page 040041. Acoustical Society of America, 2013. doi: 10.1121/1.4800944.

[2] D. K. Boyle, B. S. Henderson, and L. S. Hultgren. DGEN aeropropulsion research turbofan core/combustor-noise measurements — experiment and modal structure at core-nozzle exit. *J. Eng. Gas Turbines Power*, 143(5): 051020, 2021. doi: 10.1115/1.4049882.

[3] D. K. Boyle, B. S. Henderson, and L. S. Hultgren. DGEN aeropropulsion research turbofan core/combustor-noise measurements — experiment and modal structure at core-nozzle exit. Paper GT2020-14194, ASME Turbo Expo 2020, Virtual, Online, 2020. doi: 10.1115/GT2020-14194.

[4] L. S. Hultgren, D. K. Boyle, and B. S. Henderson. DGEN aeropropulsion research turbofan source-diagnostic test: Experimental setup and acoustic-data structure. Technical Memorandum NASA/TM-20205008042, NASA, 2020. URL https://ntrs.nasa.gov/citations/20205008042.

[5] D. K. Boyle, B. S. Henderson, and L. S. Hultgren. Core/combustor-noise baseline measurements for the DGEN aeropropulsion research turbofan. AIAA Paper 2018-3281, 24th AIAA/CEAS Aeroacoustics Conference, Atlanta, Georgia, 2018. doi: 10.2514/6.2018-3281.

[6] I. Davis and G. J. Bennett. Spatial noise source identification of tonal noise in turbomachinery using the coherence function on a modal basis. AIAA Paper 2011-2825, 17th AIAA/CEAS Aeroacoustic Conference, Portland, Oregon, 2011. doi: 10.2514/6.2011-2825.

[7] B. Pardowitz, U. Tapken, K. Knobloch, F. Bake, E. Bouty, I. Davis, and G. Bennett. Core noise — identification of broadband noise sources of a turbo-shaft engine. AIAA Paper 2014-3321, 20th AIAA/CEAS Aeroacoustics Conference, Atlanta, Georgia, 2014. doi: 10.2514/6.2014-3321.

[8] United States of America. Title 14 Code of Federal Regulations Part33 (eCFR). URL https://www.ecfr.gov/cgi-bin/text-idx?tpl=/ecfrbrowse/Title14/14cfr33_main_02.tpl.

[9] L. S. Hultgren. A first look at the DGEN380 engine acoustic data from a core-noise perspective. Technical Memorandum NASA/TM–2015-218924, NASA, 2015. URL https://ntrs.nasa.gov/citations/20150023070.

[10] D. L. Sutliff, C. A. Brown, B. Bayon, and D. Sree. Farfield acoustic characteristics of the DGEN380 turbofan engine as measured in the NASA Glenn Aero-Acoustic Propulsion Laboratory. AIAA Paper 2016-3006, 22nd AIAA/CEAS Aeroacoustic Conference, Lyon, France, 2016. doi: 10.2514/6.2016-3006.

[11] L. S. Hultgren and J. H. Miles. Noise-source separation using internal and far-field sensors for a full-scale turbofan engine. AIAA Paper 2009-3220 (NASA/TM–2009-215834), 15th AIAA/CEAS Aeroacoustic Conference, Miami, Florida, 2009. doi: 10.2514/6.2009-3220.

[12] J. S. Bendat and A. G. Piersol. *Engineering Applications of Correlation and Spectral Analysis*. Wiley-Interscience, 1980.

[13] D. K. Boyle, B. S. Henderson, and L. S. Hultgren. Transfer-function determination for infinite-tube-probe pressure transducers with application to turbofan core/combustor noise. AIAA Paper 2019-2588 (NASA/TM–2019-220045), 25th AIAA/CEAS Aeroacoustics Conference, Delft, The Netherlands, 2019. doi: 10.2514/6.2019-2588.

[14] A. M. Karchmer. Acoustic modal analysis of a full scale annular combustor. AIAA Paper 1983-0760 (NASA-TM-83334), 8th AIAA Aeroacoustics Conference, Atlanta, Georgia, 1983. doi: 10.2514/6.1983-760.

[15] B. Schuster and J. M. Mendoza. Auxiliary power unit combustion noise mesurements. Paper 2, X3-NOISE Scientific Workshop, 27–28 September, Lisbon, Portugal, 2007.

[16] C. M. Royalty and B. Schuster. Noise from a turbofan engine without a fan from the engine validation of noise and emission reduction technology (EVNERT) program. AIAA Paper 2008-2810, 14th AIAA/CEAS Aeroacoustics Conference, Vancouver, British Columbia, 2008. doi: 10.2514/6.2008-2810.

[17] E. A. Krejsa and A. M. Karchmer. Acoustic modal analysis of the pressure field in the tailpipe of a turbofan engine. Technical Memorandum NASA-TM-83387, NASA, 1983. URL https://ntrs.nasa.gov/citations/19830017228.

[18] J. H. Miles. Restricted modal analysis applied to internal annular combustor autosoectra and cross-spectra measurements. *AIAA J.*, 45(5):988–999, 2007. doi: 10.2514/1.25179.

[19] I. Davis and G. J. Bennett. Experimental investigations of coherence based noise source identfication techniques for turbomachinery applications - classic and novel techniques. AIAA Paper 2011-2830, 17th AIAA/CEAS Aeroacoustic Conference, Portland, Oregon, 2011. doi: 10.2514/6.2011-2830.

[20] G. J. Bennett, I. Davis, and U. Tapken. Broadband noise source location in turbomachinery using a conditioned spectral analysis technique coupled with modal decomposition. Paper, Inter-Noise 2010, 39th International Congress on Noise Control Engineering, Lisbon, Portugal, 2010.

[21] W. Jürgens, B. Pardowitz, L. Enghardt, and U. Tapken. Separation of broadband noise sources in aeroengine ducts with respect to modal decomposition. AIAA Paper 2011-2879, 17th AIAA/CEAS Aeroacoustics Conference, Portland, Oregon, 2011. doi: 10.2514/6.2011-2879.

[22] I. Davis and G. J. Bennett. Novel noise-source-identification technique combining acoustic modal analysis and a coherence-based noise-source-identification method. *AIAA J.*, 53(10):3088–3101, 2015. doi: 10.2514/1.J053907.

[23] P. Sijtsma, M. Dreux, B. Delescluse, R. Leneveu, and J Mardjoni. Coherent output power with groups of microphones. AIAA Paper 2024-3330, 30th AIAA/CEAS Aeroacoustic Conference, Rome, Italy, 2024. doi: 10.2514/6.2024-3330.

[24] A. Hart, K. R. Holland, and P. Joseph. Enhanching array techniques for measuring jet engine combustion noise using a modal isolation method. AIAA Paper 2018-2967, 24th AIAA/CEAS Aeroacoustics Conference, Atlanta, Georgia, 2018. doi: 10.2514/6.2018-2967.

[25] P. Rodríguez-García, K. R. Holland, and B. J. Tester. Extraction of turbofan combustion noise spectra using a combined coherence-beamforming technique. AIAA Paper 2014-3286, 20th AIAA/CEAS Aeroacoustics Conference, Atlanta, Georgia, 2014. doi: 10.2514/6.2014-3286.

[26] J. Y. Chung. Rejection of flow noise using a coherence function method. *J. Acoustical Society of America*, 62 (2):388–395, 1977.

[27] W. E. Zorumski. Aircraft noise prediction program theoretical manual, part 1. Technical Report NASA-TM-83199-PT-1, NASA, 1982. URL `https://ntrs.nasa.gov/citations/19820012072`.

[28] W. E. Zorumski. Aircraft noise prediction program theoretical manual, part 2. Technical Report NASA-TM-83199-PT-2, NASA, 1982. URL `https://ntrs.nasa.gov/citations/19820012073`.

[29] Society of Automotive Engineers International. Gas turbine jet exhaust prediction. Technical Standard (Aerospace Recommended Practice) SAE ARP876 Rev. E, 2006 (Reaffirmed 2012). doi: 10.4271/ARP876E.

[30] K. K. Ahuja. Designing clean jet-noise facilities and making accurate jet-noise measurements. *International J. Aeroacoustics*, 2(3&4):371–412, 2003. doi: 10.1260/147547203322986188.